

Parameter-free image resolution estimation based on decorrelation analysis

A. Descloux ^{*}, K. S. Größmayer  and A. Radenovic ^{*}

Super-resolution microscopy opened diverse new avenues of research by overcoming the resolution limit imposed by diffraction. Exploitation of the fluorescent emission of individual fluorophores made it possible to reveal structures beyond the diffraction limit. To accurately determine the resolution achieved during imaging is challenging with existing metrics. Here, we propose a method for assessing the resolution of individual super-resolved images based on image partial phase autocorrelation. The algorithm is model-free and does not require any user-defined parameters. We demonstrate its performance on a wide variety of imaging modalities, including diffraction-limited techniques. Finally, we show how our method can be used to optimize image acquisition and post-processing in super-resolution microscopy.

Super-resolution microscopy provides unprecedented insights into subcellular structures^{1,2}. When designing a microscopy experiment, an imaging modality for which the achievable spatiotemporal resolution matches the biological question should be selected. The image quality varies greatly among different techniques and is influenced by sample properties. Image formation can be modelled as the convolution of a ground-truth object with the specific point-spread function plus various method-related noise contributions. In Fourier space, the object spectrum is multiplied by the transfer function of the system. Its shape depends on the imaging method, but common to all techniques is image low-pass filtering, characterized by a cut-off frequency. This spatial frequency limit stated by Abbe³ is generally expressed as $k_c = NA \frac{2\pi}{\lambda}$, where NA is the numerical aperture and λ the illumination central wavelength, and corresponds to the resolution in coherent imaging.

Super-resolution techniques overcome the diffraction limit by exploiting specific fluorophore properties such as stimulated emission or temporal fluctuations. Therefore, image resolution needs to be reconsidered by taking into account the fluorescent properties of the sample⁴. Ideally, this resolution criterion should work on a single image, be independent of the imaging method, have no user-dependent settings and be compatible with classical resolution. Such an estimator of resolution is of particular interest for autonomous adaptive microscopes^{5,6} that require robust tools to automatically achieve and maintain optimal performance in long-term imaging of biological samples.

In 1982, van Heel⁷ and Saxton⁸ independently proposed Fourier ring correlation (FRC) using two independent images of the same object for resolution estimation of electron microscopy images. The idea was quickly expanded to three dimensions (3D) via Fourier shell correlation by Harauz⁹ and several threshold concepts have been proposed (0.5, 0.143 (ref. ¹⁰), 2σ (refs. ^{8,11}), spectral signal-to-noise ratio (ref. ¹²)) to extract a resolution measure. Later, Banterle¹³ and Nieuwenhuizen¹⁴ independently extended, reconsidered and applied the method to assess the resolution of single-molecule localization microscopy (SMLM) images. They define the cut-off frequency as the spatial frequency at which the so-called FRC curve drops below 0.143.

In SMLM, the two image realizations are typically accomplished by splitting the localizations into two distinct subsets. In general, it can be achieved for any imaging technique¹⁵ by acquiring two consecutive images under the same conditions. To maintain these conditions may be difficult owing to bleaching or temporal fluctuations of the fluorescence signal. This is especially pertinent in live-cell imaging and significantly challenges the stationarity assumption of FRC.

Here, we propose a new method for resolution estimation, based on an individual image without further requirements or a priori knowledge, called decorrelation analysis. The algorithm requires only a non-saturated, bandwidth-limited signal with adequate spatial sampling. This estimator is based on partial phase correlation and does not rely on any user-defined parameters. The algorithm is fast, uses only linear operations and enables the real-time objective assessment of image resolution. We successfully applied our new approach on a variety of microscopy data sets, ranging from widefield imaging to SMLM and STED microscopy. We show that our estimator can also be used to optimize image resolution, both during experiments and throughout data post-processing.

Results

Decorrelation analysis. To achieve objective threshold-free resolution estimation, we introduce a processing method termed decorrelation analysis. The main algorithm is divided into two steps. First, the Fourier transform of the image is computed after standard edge apodization to suppress high-frequency artefacts. The Fourier transform is normalized as $I_n(\mathbf{k}) = \frac{I(\mathbf{k})}{|I(\mathbf{k})|}$. The input image $I(\mathbf{k})$ and its normalized version $I_n(\mathbf{k})$ are then cross-correlated in Fourier space using Pearson correlation and condensed to a single value between 0 and 1 (Fig. 1a). Second, the operation is repeated, but the normalized Fourier transform is filtered additionally by a binary circular mask of radius $r \in [0,1]$ expressed in normalized frequencies (Fig. 1b). By repeating the calculation, we compute $d(r)$, which is expressed as:

$$d(r) = \frac{\int \text{Re}\{I(\mathbf{k})I_n^*(\mathbf{k})M(\mathbf{k};r)\}d\mathbf{k}_x d\mathbf{k}_y}{\sqrt{\int |I(\mathbf{k})|^2 d\mathbf{k}_x d\mathbf{k}_y \int |I_n(\mathbf{k})M(\mathbf{k};r)|^2 d\mathbf{k}_x d\mathbf{k}_y}}, \quad (1)$$

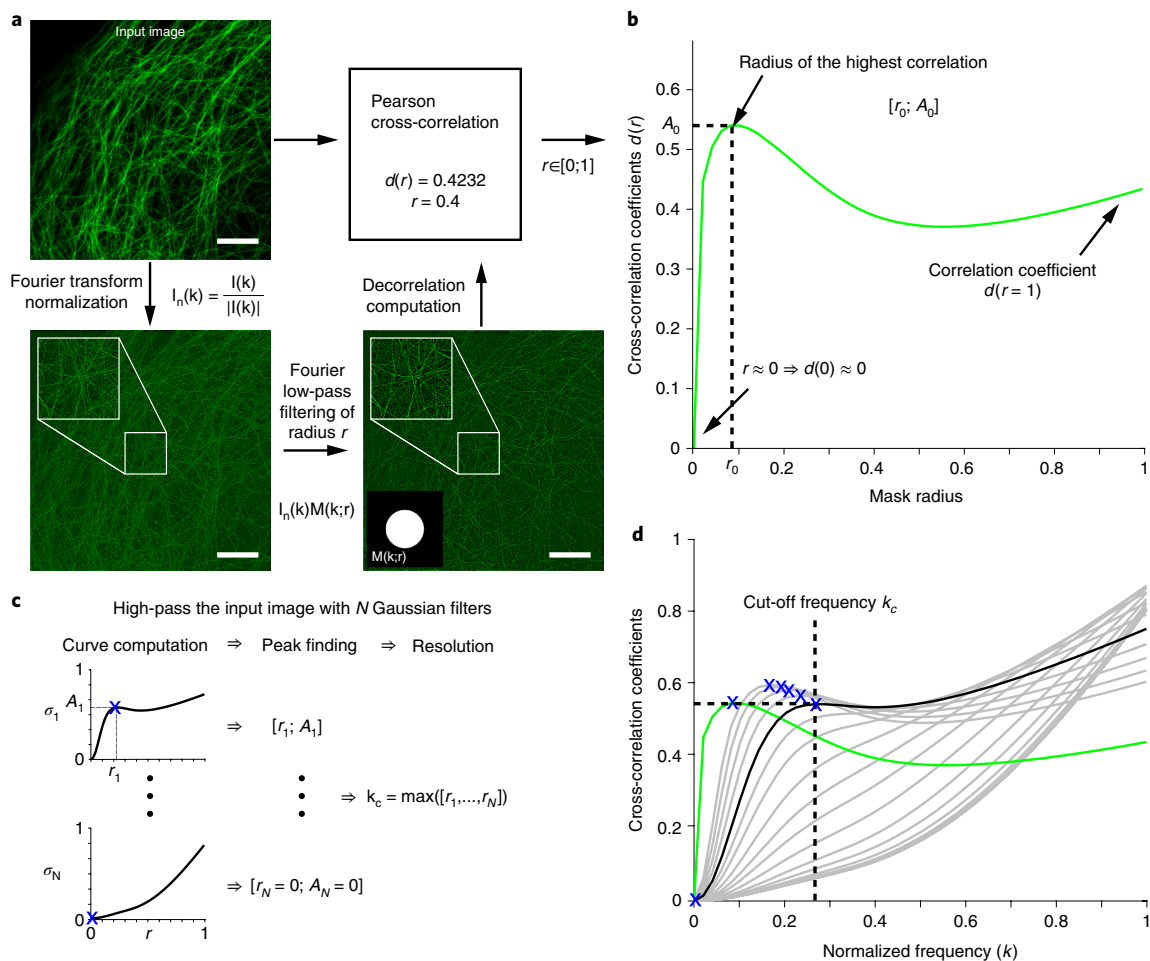


Fig. 1 | Image decorrelation analysis workflow. a, Cross-correlation of the image with its Fourier-filtered normalized version. **b**, Cross-correlation coefficient as a function of the mask radius. **c**, High-pass filtering of the input image and resolution estimation. **d**, The plot of all decorrelation functions computed for the image and resolution estimation. Green, decorrelation function without any high-pass filtering; grey, decorrelation functions with high-pass filtering; blue cross, local maxima; black, decorrelation function of highest frequency peak. Vertical dashed line, cut-off frequency k_c . Scale bar, 5 μm .

where $k = [k_x, k_y]$ denotes Fourier space coordinates $I(k)$, the Fourier transform of the input image, $I_n(k)$, the normalized Fourier transform, and $M(k;r)$, the binary mask of radius r . For a detailed mathematical derivation and additional considerations, see Supplementary Note 1.

The core idea of the method is that by normalizing the Fourier transform of the input image, we balance the signal and noise contributions while the information of the object structure is preserved in the phase (the phase is responsible for organizing the constructive and destructive interferences of the complex exponentials to form the image, the amplitude has only a minor role in this process). A binary mask radius of 1 enables the extraction of the correlation value related to the original ratio of signal and noise. If we consider an image containing only white noise, we see that $d(r=1) \approx 1$, as the white noise power spectrum is constant by definition (the normalization does not affect the signal). If we add a bandwidth-limited signal to the image, the correlation value for $r=1$ will decrease (the normalization now has a direct effect on the added signal and thus $I_n(k)$ only partially correlates with $I(k)$).

By decreasing the radius of the mask ($r < 1$), we gradually remove the noise contribution but preserve the signal owing to its bandwidth-limited nature. If the image contains only noise, the cross-correlation value will decrease linearly as a function of radius r . If we now add a signal, the decorrelation function $d(r)$ will exhibit a local maximum of amplitude A_0 that indicates the spatial frequency

r_0 of best noise rejection and signal preservation ratio. Restriction of the mask further removes more signal than noise, reducing the correlation below A_0 until it drops to 0 for $r=0$. The position r_0 of the local maximum is therefore related directly to the spatial frequency distribution of the image and its amplitude A_0 is positively correlated with the image SNR, however the use of A_0 as an SNR metric would require additional investigation. See Supplementary Note 1 for a detailed description of the algorithm and decorrelation function behaviour with respect to different noise statistics, aberrated transfer functions, cut-off frequencies, SNRs and high-pass filtering.

The position of the maximum does not indicate the resolution of the image directly, despite being related to the spatial frequency content of the image. The input image is then subjected to a total of N_g high-pass filters (from weak to very strong filtering) to attenuate the energy of low frequencies. For each filtered image, a decorrelation function is computed and the peak position r_i and amplitude A_i are extracted, generating a set of $[r_i, A_i]$ pairs (Fig. 1c). If the high-pass filtering removes too much signal, the decorrelation function will not exhibit a local maximum and the peak position and amplitude will both be set to 0. We investigated two strategies for resolution estimation (see Supplementary Note 1.2) and define the estimate as:

$$k_c = \max[r_0, \dots, r_{N_g}] \quad (2)$$

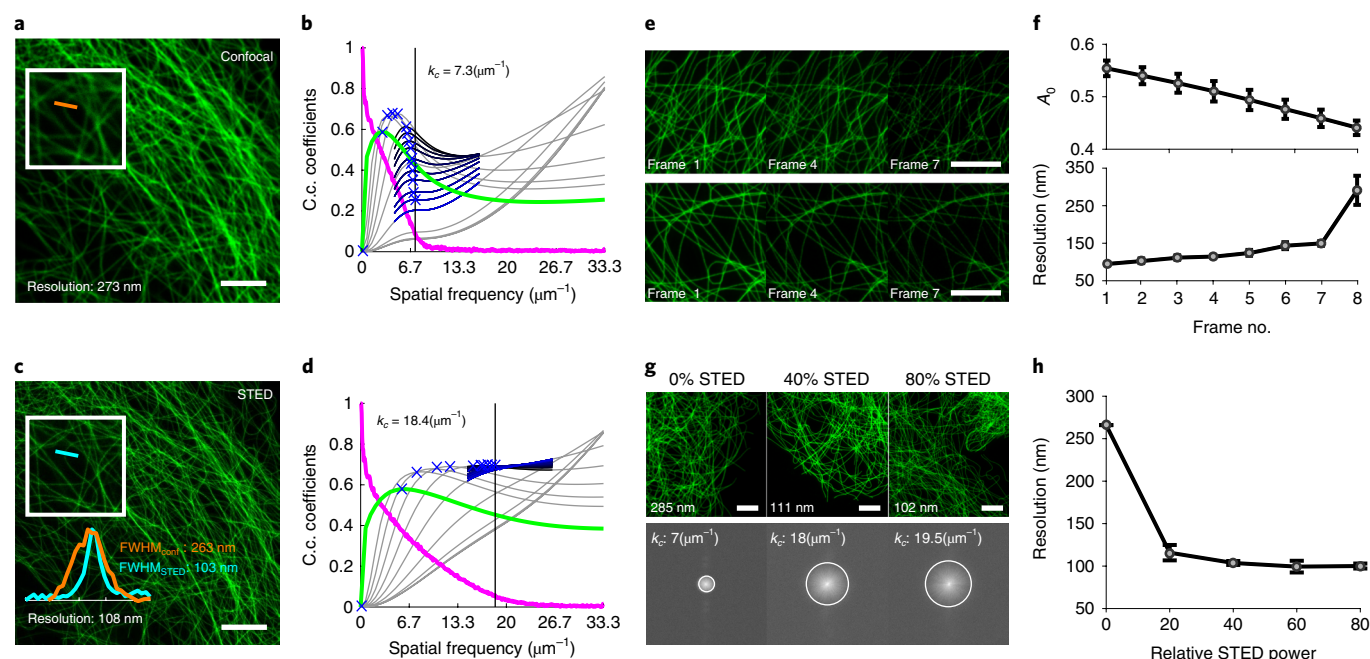


Fig. 2 | Confocal and STED. Microtubules in fixed COS-7 cells immunolabeled with Abberior Star 635P. **a,b**, Confocal image (**a**) and its corresponding decorrelation analysis (**b**). Green line, decorrelation functions before high-pass filtering; magenta line, radial average of log of absolute value of Fourier transform of **a**; gray lines, all high-pass filtered decorrelation functions; blue to black lines, decorrelation functions with refined mask radius and high-pass filtering range. Blue crosses, all local maxima. Dashed vertical line, cut-off k_c (for the sake of readability, we have used the same color and style representation for all subsequent analyses). C.c., cross-correlation. **c,d**, STED image of the same structure as in **a** with line profile of selected microtubule (**c**) and its corresponding decorrelation analysis (**d**). **e,f**, Sequential STED imaging of two different cells (**e**) and SNR estimator and resolution (average and standard deviation) (**f**) of a total of four STED sequences of different cells as a function of time. **g**, STED images as a function of STED power. The lower panel shows the corresponding Fourier space with indicated cut-off frequency. **h**, Resolution as a function of STED power (average and standard deviation of five images of different cells per STED power). Scale bar, 5 μm . Image acquisition and sample details are provided in Supplementary Table 1.

which corresponds to the local maximum of highest frequency (Fig. 1d). The resolution is then $\text{Resolution} = \frac{2 \times \text{pixel size}}{k_c}$, where k_c is expressed in normalized frequencies. By computing the resolution with varying sampling of $d(r)$ and varying number of high-pass filtering N_g , we confirm the robustness of the algorithm and estimate the precision to be ± 1 to 3 nm, independent of the type of image (see Supplementary Note 1). Simulations of point emitters, modulation transfer functions, rings and crossing lines, corroborate that our resolution estimate depends linearly on the frequency support of the image (see Supplementary Results 1.1–3) and that the amplitude of the local maximum A_0 before any filtering is directly correlated with the image SNR.

Instead of searching for the frequency at which the transfer function vanishes (only possible in the absence of noise), we estimate the highest frequency from the local maxima of the decorrelation functions, enabling parameter-free image resolution estimation. The presented method does not estimate the theoretical resolution as stated by Abbe, but the highest frequency with sufficiently high signal in relation to noise. It provides a rapid and objective method by which to quantify the frequency content of a single image without any user-defined parameter.

Demonstrations of decorrelation analysis. To demonstrate the validity and broad applicability of the method, we processed DNA origami nanorulers with different geometries¹⁶ provided by GATTAquant (courtesy of P. Tinnefeld and J. Schmied). The resolutions estimated by our algorithm are smaller than the mark-to-mark distances of the nanorulers, which corroborates the fact that they are resolved in all imaging modalities (see Supplementary Results 2). After establishing the validity of our method using DNA origami, we extended our analysis to various diffraction-limited (see

Supplementary Results 3 for bright-field imaging, Supplementary Results 4 for super-resolution optical fluctuation imaging and Results 5 for deconvolution and post-processing) and super-resolution microscopy images of biological structures. We further validated our resolution estimates by imaging z-stacks of fluorescent beads. Our estimator provides a unique tool to assess the alignment of optical setups or the performance of microscope objectives using a single experimental image (see Supplementary Note 2). All results were processed using custom open source MATLAB code. For ease of use, the algorithm is also available as an open source ImageJ¹⁷ plugin (see Supplementary Note 3 and Code Availability statement).

Confocal and STED. Confocal¹⁸ and stimulated emission depletion (STED) microscopy^{19,20} are point-scanning techniques that can be realized with the same setup, enabling the transition from diffraction-limited to super-resolution imaging. STED microscopy is a super-resolution method that uses confocal illumination for excitation and a doughnut-shaped depletion beam to de-excite the surrounding fluorophores prior to fluorescence emission. The resolution of STED microscopy for a given fluorophore depends on the spatial and temporal co-alignment of the two beams²¹, the shape, and the quality of the depletion beam and its power²².

We imaged the microtubule network of COS-7 cells both in confocal and pulsed STED mode. Figure 2a–d shows the resulting images and their corresponding decorrelation analysis.

As expected, all decorrelation functions exhibit a local maximum, with STED showing a 2.52-fold resolution improvement over confocal imaging. We plotted the manually selected line profile of a microtubule cross-section (Fig. 2c), a method typically used to estimate the resolution. The measured full width half maxima are in good agreement with our estimates.

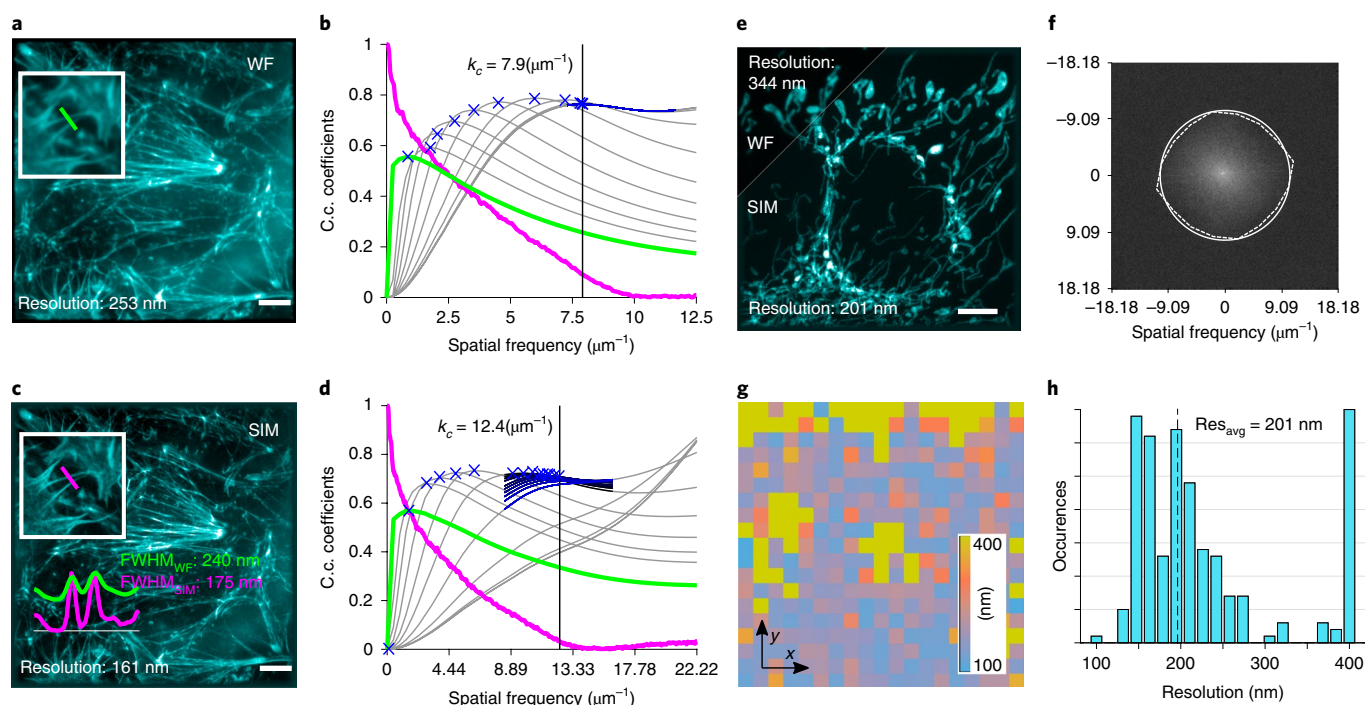


Fig. 3 | Widefield imaging and structured illumination microscopy. **a**, Pseudo-widefield (WF) image (average of the SIM sequence) of the actin network in fixed U2OS cells labeled with phalloidin Atto 488 (Courtesy of T. Huser). **b**, Corresponding decorrelation analysis. **c**, SIM reconstruction of **a** with selected cross sections. **d**, Corresponding decorrelation analysis. **e**, Pseudo- and SIM reconstruction of mitochondria network in U2OS cells labeled with mitotracker. **f**, Sectorial resolution estimation (dashed white line) and average resolution (solid white circle). **g**, Local resolution estimate of **e** in tiles of 70×70 pixels with an overlap of 20 pixels. **h**, Histogram of local resolution shown in **g**. Dashed line indicates the median resolution. Scale bar, $5 \mu\text{m}$. Image acquisition and sample details are provided in Supplementary Table 1.

Figure 2e,f shows the result of the analysis performed on a time series of eight consecutive STED images. As expected, repeated imaging of the same structure gradually bleaches the fluorophores, progressively degrading the SNR as indicated by the parameter A_0 . We also observe a consistent deterioration of the resolution until the seventh frame, where we reach a resolution close to confocal imaging. The bleaching is so strong that the structure is no longer continuous. The proposed method confirms the expected degradation of image resolution and provides an estimate of the image SNR and resolution (see Supplementary Results 6). Figure 2g,h illustrates how our resolution estimation can be used to optimize STED imaging. Imaging under several STED illumination powers was performed, with adjustment of the excitation power to maintain the optimal dynamic range of the image to avoid noise limitation of STED resolution¹⁵. Using 20% STED laser power shows a significant improvement of the resolution (~ 2.4 -fold) but further doubling of the power only decreases the resolution by a factor of 1.1, as expected, owing to the non-linear behaviour of STED. Further increases in STED power do not lead to significant changes in resolution, possibly owing to misalignment of the excitation and STED beam, imperfect 'zero' of the STED doughnut as well as excess photo-bleaching and background induced by the STED beam²⁰. We conducted additional experiments, to investigate more acquisition parameters, such as the STED delay and pixel size, and to compare the performance of different dyes to choose the optimal label (see Supplementary Results 6). Our algorithm provides a direct and straightforward estimation of image resolution to objectively identify the best acquisition settings and optimize sample preparation based on a single image of the sample of interest without imposing additional requirements on the data acquisition scheme. In principle, it should be possible to use our resolution estimate to tune the microscope alignment; for example, to adjust the overlap of the STED doughnut with the confocal excitation spot.

Widefield imaging and structured illumination microscopy.

High-resolution live-cell STED imaging has been performed, but care should be taken to avoid sample damage due to high-depletion laser powers²⁰. A super-resolution method that is widely used for imaging dynamics of living cells is structured illumination microscopy^{23–25} (SIM). SIM aims to improve the lateral and axial resolution by multiple imaging of the sample with high-frequency illumination patterns²⁶. The theoretical resolution improvement of SIM is linked to the illumination spatial frequency. In practice, SIM resolution depends on refractive index mismatch, the pattern modulation contrast and local distortion²⁷. Figure 3a shows a pseudo-widefield image of actin filaments in U2OS cells²⁸ obtained on a commercial SIM instrument (courtesy of T. Huser). A resolution of approximately 253 nm is estimated by decorrelation analysis (see Fig. 3b). Figure 3c shows the SIM reconstruction (see Supplementary Note 4), and its corresponding decorrelation analysis is shown in Fig. 3d, which estimates a 1.56-fold improved resolution of 161 nm. Measurement of the position of the illumination peaks in the Fourier transform of the raw data (4.75 and $9.5 \mu\text{m}^{-1}$ for the first and second diffraction order, respectively), provides a method by which to estimate the theoretically expected resolution improvement. We observe that the contribution of the first diffraction order with widefield resolution ($\frac{7.9+4.75}{7.9} \approx 1.6$) fits well with our estimation, which indicates that the information encoded in the second diffraction order is not sufficiently contrasted. The use of more advanced reconstruction algorithms may improve this result.

So far, we have considered only the global resolution; that is, averaged over the whole image. To account for non-isotropic resolution, we subdivide the Fourier space into sectors and compute the cut-off frequency as a function of the direction (sectorial resolution, see Supplementary Note 5). Figure 3e shows a pseudo-widefield and SIM reconstruction of mitochondria²⁸ in U2OS cells

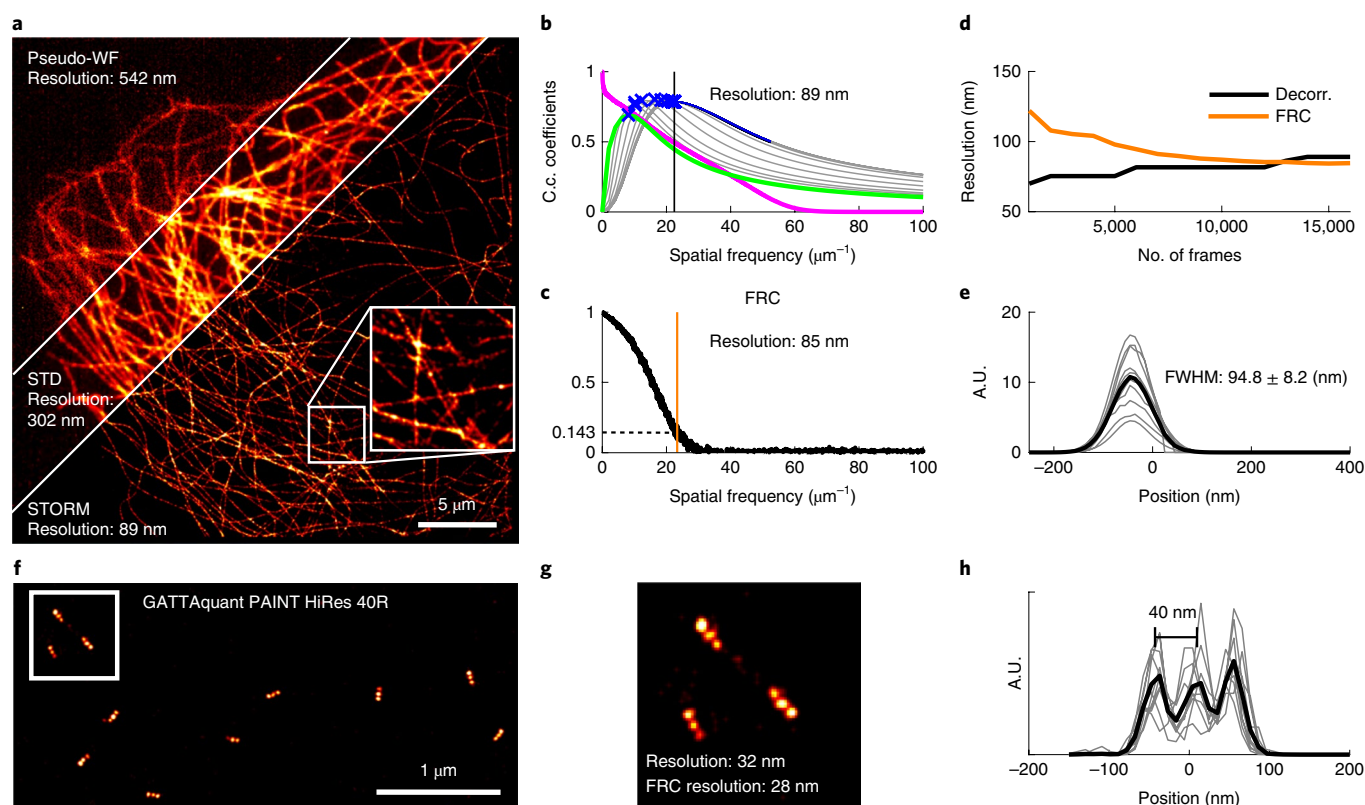


Fig. 4 | Localization microscopy. (a) Pseudo-WF, standard deviation (STD) and STORM images of microtubules in COS-7 cells labelled with Abberior Flip 565 based on 16,000 frames. **b**, Decorrelation analysis of **a**. **c**, FRC analysis of **a**. **d**, Decorrelation resolution (black line) and FRC resolution (orange line) as a function of the number of frames. **e**, Line profile of 15 randomly selected microtubule cross-sections. **f**, GATTAquant PAINT image of HiRes 40R nanoruler with mark-to-mark distances of 40 nm. **g**, Zoomed-in image of section marked in **f**, and decorrelation and FRC resolution estimate. **h**, Ten line profiles of HiRes 40R molecules indicating a resolution that is higher than 40 nm. Image acquisition and sample details are provided in Supplementary Table 1.

measured on a different commercial microscope (courtesy of M. Sauer, resolution gain of 1.73). Figure 3f displays the Fourier transform of the SIM reconstruction, overlapped with the sectorial and average resolution.

By subdividing the image into smaller tiles (as for FRC in ref. ¹⁴), we can estimate the resolution over the whole field of view and reveal local variations in resolution (Fig. 3g). Owing to the very weak signal in Fig. 3e (top and center), corresponding subregions have large resolution values. To preserve the dynamic range, all resolutions higher than 400 nm were set to 400 nm. Furthermore, the resolution map can be plotted as a histogram (Fig. 3h), providing yet another perspective. We also see that the average resolution is approximately the median of all local resolutions.

Single-molecule localization microscopy. Finally, we applied our method to single-molecule localization microscopy^{29–31} data. In this case, super resolution is achieved by the individual localization of a subset of sparsely and stochastically blinking emitters in successive image frames. By fitting the emission point-spread functions, single- and multiple-emitter positions can be determined with nanometric accuracy^{32,33}. To estimate the resolution, our method requires a rendered image. We validated, using simulations, that our algorithm is able to correctly estimate the resolution in SMLM (see Supplementary Results 7). Figure 4a shows a dSTORM (direct stochastic optical reconstruction microscopy) image based on 16,000 frames of Abberior Flip 565 immuno-labelled microtubules in COS-7 cells.

With self-blinking dyes^{34,35}, it is not possible to take a widefield image. We therefore obtained a pseudo-widefield and standard deviation image by computing the temporal average and standard

deviation of all frames. We estimate a resolution of 542 nm for wide-field imaging owing to the low SNR of the image, 302 nm for the standard deviation image and 89 nm for the STORM image. Figure 4b,c displays the corresponding decorrelation analysis and FRC curve. Both estimates agree on the resolution, with FRC (estimated resolution of 85 nm) being slightly more optimistic, consistent with the behaviour observed in simulations and reported recently by Marsh et al.³².

Figure 4d shows how our method and FRC resolution vary as a function of the number of frames. We observe a marked difference in the predicted resolution only up to 5,000 frames. For a low number of frames, the localization events in the two split FRC images are too sparse to produce significant correlations, leading to a large resolution estimate. However, our method considers only a single image, consisting of sparse Gaussians with no apparent structure but excellent SNR (rendered localization image without noise). This leads to a very optimistic resolution estimate with the localization uncertainty as a lower bound. As we increase the number of frames, the two random subsets of localization events start to correlate and the FRC resolution estimate decreases. Similarly, as we include more localization events, a larger-scale structure (containing low spatial frequencies) emerges. Consequently, our resolution estimate increases as the structure is built up. We observe that both methods converge at approximately the same speed at around 12,000 frames, with FRC estimating a slightly higher resolution³⁶. Figure 4e shows randomly selected microtubule cross sections. The apparent average microtubule diameter of approximately 95 nm is consistent with the resolution estimate and secondary immunostaining, which increases the apparent microtubule diameter by 10–30 nm (refs. ^{37,38}).

Figure 4f displays an image of GATTAquant HiRes 40R nanorulers³⁹ (courtesy of P. Tinnefeld and J. Schmied). The close up of three molecules (Fig. 4g) as well as line profiles of individual molecules (Fig. 4h) show that the three-point source spaced by 40 nm can be resolved. Our algorithm estimates a resolution of 32 nm, whereas FRC estimates a resolution of 28 nm, again slightly more optimistic.

Finally, it has been shown that multiple blinking events can severely impact the FRC resolution estimate by introducing spurious correlations¹⁴. Although this effect can be mitigated in principle, it requires an accurate estimation of the underlying blinking statistics⁴⁰. Our resolution estimate is independent of the probability of multiple blinking (see Supplementary Results 7).

Discussion

We developed decorrelation analysis for parameter-free resolution and SNR estimation of a single microscopy image. We were able to circumvent the need for a threshold by introducing a new form of partial phase correlation. In principle, our method can be applied to any imaging technique, including electron microscopy, atomic force microscopy, X-ray tomography and live-cell imaging. Here, we have demonstrated its broad applicability to various types of microscopy images, ranging from brightfield to single-molecule localization microscopy images. By processing DNA origami nanoruler data, we showed that the method can be used to quantitatively assess the resolution that enabled an optimization of imaging parameters, post-processing and reconstruction. Our approach provides a new and objective way to quantify the effective resolution in super-resolution microscopy that is less sensitive to common imaging artifacts than existing approaches. The extension of our method to 3D would require a reformulation of our algorithm in spherical coordinates.

By developing an open-source ImageJ plug-in, we enable non-image-processing specialists to use our method. We provide a unique and novel approach for resolution estimation based on the analysis of a single image that can be used for image processing optimization and image reconstruction comparison. We envisage that our new resolution estimate will provide a powerful tool for on-the-fly microscopy setup characterization and optimization as well as for automated microscopes.

Online content

Any methods, additional references, Nature Research reporting summaries, source data, statements of code and data availability and associated accession codes are available at <https://doi.org/10.1038/s41592-019-0515-7>.

Received: 10 December 2018; Accepted: 15 June 2019;
Published online: 26 August 2019

References

- Sahl, S. J., Hell, S. W. & Jakobs, S. Fluorescence nanoscopy in cell biology. *Nat. Rev. Mol. Cell Biol.* **18**, 685–701 (2017).
- Sigal, Y. M., Zhou, R. & Zhuang, X. Visualizing and discovering cellular structures with super-resolution microscopy. *Science* **361**, 880–887 (2018).
- Abbe, E. Beiträge zur Theorie des Mikroskops und der mikroskopischen Wahrnehmung. *Arch. für. Mikrosk. Anat.* **9**, 413–418 (1873).
- Sheppard, C. J. R. Resolution and super-resolution. *Microsc. Res. Tech.* **80**, 590–598 (2017).
- Power, R. M. & Huisken, J. Adaptable, illumination patterning light sheet microscopy. *Sci. Rep.* **8**, 1–11 (2018).
- Štefko, M., Ottino, B., Douglass, K. M. & Manley, S. Autonomous illumination control for localization microscopy. *Opt. Express* **26**, 30882–30900 (2018).
- Heel, M. Van Similarity measures between images. *Ultramicroscopy* **21**, 95–100 (1987).
- Saxton, W. & Baumeister, W. The correlation averaging of a regularly arranged bacterial cell envelope protein. *J. Microsc.* **127**, 127–138 (1982).
- Haraux, G. & van Heel, M. Exact filters for general geometry three dimensional reconstruction. *Optik* **78**, 146–156 (1986).
- Rosenthal, P. B. & Henderson, R. Optimal determination of particle orientation, absolute hand, and contrast loss in single-particle electron cryomicroscopy. *J. Mol. Biol.* **333**, 721–745 (2003).
- Orlova, E. V. et al. Structure of keyhole limpet hemocyanin type 1 (KLH1) at 15 Å resolution by electron cryomicroscopy and angular reconstitution. *J. Mol. Biol.* **271**, 417–437 (1997).
- Unser, M., Trus, B. L. & Steven, A. C. A new resolution criterion based on spectral signal-to-noise ratio. *Ultramicroscopy* **23**, 39–52 (1987).
- Banterle, N., Bui, K. H., Lemke, E. A. & Beck, M. Fourier ring correlation as a resolution criterion for super-resolution microscopy. *J. Struct. Biol.* **183**, 363–367 (2013).
- Nieuwenhuizen, R. P. J. et al. Measuring image resolution in optical nanoscopy. *Nat. Methods* **10**, 557–562 (2013).
- Tortarolo, G., Castello, M., Diaspro, A., Koho, S. & Vicidomini, G. Evaluating image resolution in stimulated emission depletion microscopy. *Optica* **5**, 32 (2018).
- Raab, M. et al. Using DNA origami nanorulers as traceable distance measurement standards and nanoscopic benchmark structures. *Sci. Rep.* **8**, 1780 (2018).
- Abramoff, M. D., Magalhães, P. J. & Ram, S. J. Image processing with ImageJ. *Biophotonics Int.* **11**, 36–42 (2004).
- Minsky, M. Memoir on inventing the confocal scanning microscope. *Scanning* **10**, 128–138 (1988).
- Hell, S. W. & Wichmann, J. Breaking the diffraction resolution limit by stimulated emission: stimulated-emission-depletion fluorescence microscopy. *Opt. Lett.* **19**, 780 (1994).
- Vicidomini, G., Bianchini, P. & Diaspro, A. STED super-resolved microscopy. *Nat. Methods* **15**, 173–182 (2018).
- Tortarolo, G., Sun, Y., Teng, W., Ishitsuka, Y. & Vicidomini, G. Photon-separation to enhance the spatial resolution of pulsed STED microscopy. *Nanoscale* **11**, 1754–1761 (2019).
- Westphal, V. & Hell, S. W. Nanoscale resolution in the focal plane of an optical microscope. *Phys. Rev. Lett.* **94**, 1–4 (2005).
- Heintzmann, R. & Cremer, C. G. Laterally modulated excitation microscopy: improvement of resolution by using a diffraction grating. (International Society for Optics and Photonics, 1999).
- Frohn, J. T. *Super-resolution fluorescence microscopy by structured light illumination*. PhD thesis, ETH Zürich (2000).
- Gustafsson, M. G. L. Surpassing the lateral resolution limit by a factor of two using structured illumination microscopy. *J. Microsc.* **198**, 82–87 (2000).
- Heintzmann, R. & Huser, T. Super-resolution structured illumination microscopy. *Chem. Rev.* **117**, 13890–13908 (2017).
- Demmerle, J. et al. Strategic and practical guidelines for successful structured illumination microscopy. *Nat. Protoc.* **12**, 988–1010 (2017).
- Müller, M., Mönkemöller, V., Hennig, S., Hübner, W. & Huser, T. Open-source image reconstruction of super-resolution structured illumination microscopy data in ImageJ. *J. Nat. Commun.* **7**, 1–6 (2016).
- Rust, M. J., Bates, M. & Zhuang, X. W. Sub-diffraction-limit imaging by stochastic optical reconstruction microscopy (STORM). *Nat. Methods* **3**, 793–795 (2006).
- Betzig, E. et al. Imaging intracellular fluorescent proteins at nanometer resolution. *Science* **313**, 1642–1645 (2006).
- Sauer, M. & Heilemann, M. Single-molecule localization microscopy in eukaryotes. *Chem. Rev.* **117**, 7478–7509 (2017).
- Marsh, R. J. et al. Artifact-free high-density localization microscopy analysis. *Nat. Methods* **15**, 689 (2018).
- Legant, W. R. et al. High-density three-dimensional localization microscopy across large volumes. *Nat. Methods* **13**, 359–365 (2016).
- Fölling, J. et al. Photochromic rhodamines provide nanoscopy with optical sectioning **. *Angew. Chem. Int. Ed. Engl.* **46**, (6266–6270) (2007).
- Bossi, M. et al. Multicolor far-field fluorescence nanoscopy through isolated detection of distinct molecular species. *Nano Lett.* **8**, 2463–2468 (2008).
- Lambert, T. J. & Waters, J. C. Navigating challenges in the application of superresolution microscopy. *J. Cell Biol.* **216**, 53–63 (2016).
- Mikhaylova, M. et al. Resolving bundled microtubules using anti-tubulin nanobodies. *Nat. Commun.* **6**, 1–7 (2015).
- Pleiner, T., Bates, M. & Görlich, D. A toolbox of anti-mouse and anti-rabbit IgG secondary nanobodies. *J. Cell Biol.* **217**, 1143–1154 (2017).
- Schmied, J. J. et al. Fluorescence and super-resolution standards based on DNA origami Flaws in evaluation schemes for pair- input computational predictions. *Nat. Methods* **9**, 1133–1134 (2012).
- Annibale, P., Vanni, S., Scarselli, M., Rothlisberger, U. & Radenovic, A. Quantitative photo activated localization microscopy: unraveling the effects of photoblinking. *PLoS ONE* **6**, e22678 (2011).

Acknowledgements

The authors would like to thank T. Lukes and T. Laser for insightful discussions. We also thank H. Deschout, M. Muller, T. Huser and M. Sauer for sharing SOFI and SIM data.

We also thank J. Schmied and P. Tinnefeld for sharing GATTAquant nanoruler data and N. Bantherle and A. Planchette for proofreading. This project has been funded in part by the Horizon 2020 research and innovation program of the European Union via grant 686271/SEFRI 16.0047. K.S.G. acknowledges support from the Horizon 2020 Framework Program of the European Union under the Marie Skłodowska-Curie grant agreement no. 750528 and thanks the NVIDIA Corporation for the donation of a Titan Xp GPU. A.D. and A.R. acknowledge support from the Zeiss IDEAS center. We would like to thank the EPFL BioImaging & Optics Core Facility (EPFL-BIOP) for access to confocal and STED microscopes.

Author contributions

A.D. proposed and developed the method, processed all of the presented data, and wrote the MATLAB and Java code. K.S.G. prepared all of the cells and performed measurements. A.R. supervised the research. A.D. wrote the manuscript with comments of all co-authors at all stages.

Competing interests

The authors declare no competing interests.

Additional information

Supplementary information is available for this paper at <https://doi.org/10.1038/s41592-019-0515-7>.

Reprints and permissions information is available at www.nature.com/reprints.

Correspondence and requests for materials should be addressed to A.D. or A.R.

Peer review information: Rita Strack was the primary editor on this article and managed its editorial process and peer review in collaboration with the rest of the editorial team.

Publisher's note: Springer Nature remains neutral with regard to jurisdictional claims in published maps and institutional affiliations.

© The Author(s), under exclusive licence to Springer Nature America, Inc. 2019

Methods

Cell culture. HeLa and COS-7 cells were cultured at 37 °C and 5% CO₂ using DMEM high glucose with pyruvate (4.5 g l⁻¹ glucose, with GlutaMAX supplement) supplemented with 10% fetal bovine serum and 1× penicillin-streptomycin (all gibco, Thermo Fisher Scientific).

Cell fixation and immunostaining. Cells were seeded in Lab-tek II chambered cover slides (nunc) or on 18 mm high-precision no. 1.5 borosilicate coverslips (Marienfeld) in 12-well plates (Thermo Fisher Scientific) 1–2 d before fixation in DMEM (see cell culture) or DMEM high glucose without phenol red (4.5 g l⁻¹ glucose) supplemented with 4 mM L-glutamine, 10% fetal bovine serum and 1× penicillin-streptomycin (all gibco, Thermo Fisher Scientific).

HeLa cells. Cells were washed twice in pre-warmed buffer (microtubule stabilizing buffer (MTSB); 100 mM PIPES buffer pH 6.8, 2 mM MgCl₂, 5 mM EGTA or PBS for wheat germ agglutinin (WGA) staining), followed by application of pre-warmed fixation buffer (3.7% paraformaldehyde (PFA), 0.2% Triton X-100 in MTSB or 3.7% PFA in PBS for WGA staining) for 15 min at room temperature (~23 °C). Cells were then washed three times for 5 min each with 1× PBS and stored in 50% glycerol in 1× PBS at 4 °C or the immunostaining protocol was continued to prepare samples for fluorescence imaging. Fixed and permeabilized cells were blocked with 3% BSA in 1× PBS and 0.05% Triton X-100 for 60 min at room temperature or overnight at 4 °C.

Cells fixed without permeabilization were stained with 5 ng ml⁻¹ WGA-Atto 565 for 10 min followed by three times 5 min washes with 1× PBS. The blocked samples with prior permeabilization were immediately incubated with a mix of primary anti-tubulin antibody (1 mg ml⁻¹ DM1a mouse monoclonal (ab80779) 1:150 dilution, Abcam) in antibody incubation buffer (AIB; 1% BSA in 1× PBS and 0.05% Triton X-100) for 60 min at room temperature. Cells were then washed three times for 5 min each with AIB, followed by incubation with donkey anti-mouse Alexa Fluor 647 antibody (0.005 mg ml⁻¹, Invitrogen) for 60 min at room temperature. This and all subsequent steps were performed in the dark. All cells were again washed three times for 5 min each with AIB and incubated for 15 min post-fixation with 2% PFA in 1× PBS followed by three 5 min washes with PBS. Cells were imaged immediately or stored in 50% glycerol in 1× PBS at 4 °C until imaging.

COS-7 cells. The protocol is similar to that described previously by Chazeau et al.⁴¹. Cells were washed twice in pre-warmed DMEM without phenol red (see cell culture) following 90 s incubation with extraction buffer (MTSB; 80 mM PIPES, 7 mM MgCl₂, 1 mM EGTA, 150 mM NaCl, 5 mM D-glucose, adjusted to pH 6.8 using KOH) with freshly added 0.3% Triton X-100 (AppliChem) and 0.25% glutaraldehyde (stock solution 50% electron microscopy grade, Electron Microscopy Sciences). Immediately afterwards, pre-warmed PFA in PBS was incubated for 15 min at room temperature. Cells were then washed three times for 5 min each with 1× PBS and stored in 50% glycerol in 1× PBS at 4 °C or the immunostaining protocol was continued. Next, a freshly prepared solution of 10 mM NaBH₄ in 1× PBS was incubated on the cells for 7 min followed by one quick wash in 1× PBS, and two washes for 10 min in 1× PBS on an orbital shaker. Cells were permeabilized in PBS with 0.25% Triton X-100 for 7 min followed by blocking with blocking buffer (2% (w/v) BSA, 10 mM glycine, 50 mM ammonium chloride NH₄Cl in PBS pH 7.4 for 60 min at room temperature or overnight at 4 °C.

The blocked samples were incubated immediately with primary anti-tubulin antibody (clone B-5-1-2 ascites fluid 1:100–1:200 dilution, Sigma-Aldrich) in blocking buffer for 60 min at room temperature. Cells were then washed three times for 5 min each with blocking buffer, followed by incubation with either donkey anti-mouse Alexa Fluor 647 antibody for super-resolution optical fluctuation imaging (SOFI) (donkey anti-mouse (H+L) highly cross-adsorbed at 0.005 mg ml⁻¹, Invitrogen), donkey anti-mouse Abberior Flip 565 for SMLM imaging (preparation as below at 1:200 dilution) or goat anti-mouse Abberior Star 635P (at 0.005–0.01 mg ml⁻¹, Abberior), goat anti-mouse Atto 594 (at 0.0025–0.005 mg ml⁻¹, Atto-tec), donkey anti-mouse Alexa Fluor 594 antibody (donkey anti-mouse (H+L) highly cross-adsorbed at 0.005 mg ml⁻¹, Invitrogen) or donkey anti-mouse biotin (Biotin-SP (long spacer) AffiniPure Donkey Anti-Mouse IgG (H+L), at 1:200, Jackson ImmunoResearch) for STED imaging for 60 min at room temperature. This and all subsequent steps were performed in the dark. All cells were again washed three times for 5 min each with AIB and incubated for 15 min post-fixation with 2% PFA in 1× PBS followed by three 5 min washes with PBS. Cells with biotinylated secondary antibody were additionally incubated with streptavidin Atto 490LS (at 0.01 mg ml⁻¹, Atto-tec) in PBS for 30 min followed by three washes for 5 min in PBS before post-fixation. Cells were imaged immediately or stored in 50% glycerol in 1× PBS at 4 °C until SOFI or SMLM imaging. For STED microscopy, cells were mounted on a coverglass slide (Thermo Fisher Scientific) using Mowiol-DABCO (for preparation, see below) and allowed to harden for at least 24 h at room temperature. Cells were imaged within 1 week of sample preparation.

Preparation of labeled proteins. Donkey anti-mouse (H+L) highly cross-adsorbed antibody (2 mg ml⁻¹, Invitrogen) was incubated with Abberior Flip 565-NHS (Abberior) and 2 mg ml⁻¹ WGA (Vector Labs) was incubated with Atto565-NHS ester (Atto-tec) at a ratio of 1: 6 for 1 h at room temperature while shaking with the pH raised to 8.3 using sodium bicarbonate. The mixture was purified using illustra NAP Columns (GE Healthcare) according to the manufacturer's instructions and eluted with slightly acidic PBS to recover the labeled antibody at neutral pH. The protein concentration was estimated by absorption spectrometry at <1.5 mg ml⁻¹ donkey anti-mouse Abberior Flip 565 and 0.5 mg ml⁻¹ WGA Atto 565.

Imaging buffer and embedding medium. The samples for SOFI using Alexa Fluor dyes were imaged in a 50 mM Tris-HCl pH 8.0, 10 mM NaCl buffer containing an enzymatic oxygen scavenging system (2.5 mM protocatechuic acid (PCA) and 50 nM protocatechuate-3,4-dioxygenase from *Pseudomonas* Sp. (PCD) with >3 units m g⁻¹) and a thiol (2-mercaptoethylamine). The thiol and a stock solution of 100 mM PCA in water, pH adjusted to 9.0 with NaOH, were always prepared fresh. PCD was aliquoted at a concentration of 10 µM in storage buffer (100 mM Tris-HCl pH 8.0, 50% glycerol, 50 mM KCl, 1 mM EDTA) at -20 °C and thawed immediately before use. The samples for SMLM using Abberior Flip 565 were imaged in 1× PBS. Mowiol-DABCO for STED embedding was prepared according to the manufacturer's protocol (Roth Gebrauchsanweisung Mowiol 488). Aliquots were kept at -20 °C and thawed immediately before use.

Microscope setups. *Widefield imaging, SOFI and SMLM.* Data for Fig. 4a, Supplementary Results Figs. 4.1e–g and 5.1, and Supplementary Note Fig. 2.1 were acquired on a standard widefield custom built microscope. A total of 4 illumination laser lines (405 nm 200 mW, Roithner; 488 nm 200 mW, Toptica; 561 nm 350 mW, Laser Quantum; 635 nm 1 W, Roithner) are collimated, expanded and combined with dichroic filters. The beams are then cropped with a rectangular aperture of approximately 7.2 mm placed in the conjugated object plane, resulting in a 120×120 µm field of view. The beams are then focused with an achromatic lens (f=200 mm) and reflected by a 3 mm thick Quad Line Beamsplitter (R405/488/561/635; Semrock) in the back focal plane of the objective (Nikon 60×/1.27NA SR water immersion). The fluorescence signal is focused on the camera (Orca Flash 4.0, Hamamatsu) with a 200 mm achromatic lens. The sample position is controlled in X and Y by a Scan-plus IM 120×80 (Marzhauser) and in Z by a Nano-Z piezo nanopositioner (Mad City Labs). All acquisitions were performed using Micromanager. The laser intensities used in the experiments can be found in Supplementary Table 1.

Confocal and STED microscopy. Confocal and STED microscopy was performed at the Ecole polytechnique fédérale de Lausanne (EPFL) bioimaging and optics platform (BIOP) using a Leica SP8 STED 3X. The setup consists of a Leica DMi 8 inverted microscope body equipped with a white light laser (470–670 nm) and a Leica HC PL APO 100×/1.40 oil objective for STED. For STED imaging we used the 775 nm pulsed depletion laser and detected the fluorescence on HyD detectors. Laser power of 100% at 775 nm corresponds to 403 mW, laser power of 100% 633 nm corresponds to 1.12 mW, laser power of 100% 488 nm corresponds to 0.33 mW and laser power of 100% 520 nm corresponds to 0.43 mW (power measurements were performed after the objective by the BIOP). The laser powers and other acquisition parameters used in the experiments can be found in Supplementary Table 1.

Data processing. The algorithm is implemented in MATLAB (Mathworks) and ImageJ. All the codes are available upon request.

Reporting Summary. Further information on research design is available in the Nature Research Reporting Summary linked to this article.

Data availability

All data needed to evaluate the conclusions in the paper are present in the paper and/or the Supplementary Results and Notes. Additional data related to this paper may be requested from the authors.

Code availability

The MATLAB source code, the ImageJ plugin and the source Java code are publicly available on <https://github.com/Ades91/ImDecorr.git> or may be requested from the authors.

References

- Chazeau, A., Katrukha, E. A., Hoogenraad, C. C. & Kapitein, L. C. Studying neuronal microtubule organization and microtubule-associated proteins using single molecule localization microscopy. *Methods Cell Biol.* **131**, 127–149 (2016).

Reporting Summary

Nature Research wishes to improve the reproducibility of the work that we publish. This form provides structure for consistency and transparency in reporting. For further information on Nature Research policies, see [Authors & Referees](#) and the [Editorial Policy Checklist](#).

Statistics

For all statistical analyses, confirm that the following items are present in the figure legend, table legend, main text, or Methods section.

n/a Confirmed

- ☐ ☒ The exact sample size (n) for each experimental group/condition, given as a discrete number and unit of measurement
- ☐ ☒ A statement on whether measurements were taken from distinct samples or whether the same sample was measured repeatedly
- ☒ ☐ The statistical test(s) used AND whether they are one- or two-sided
Only common tests should be described solely by name; describe more complex techniques in the Methods section.
- ☒ ☐ A description of all covariates tested
- ☒ ☐ A description of any assumptions or corrections, such as tests of normality and adjustment for multiple comparisons
- ☐ ☒ A full description of the statistical parameters including central tendency (e.g. means) or other basic estimates (e.g. regression coefficient) AND variation (e.g. standard deviation) or associated estimates of uncertainty (e.g. confidence intervals)
- ☒ ☐ For null hypothesis testing, the test statistic (e.g. F , t , r) with confidence intervals, effect sizes, degrees of freedom and P value noted
Give P values as exact values whenever suitable.
- ☒ ☐ For Bayesian analysis, information on the choice of priors and Markov chain Monte Carlo settings
- ☒ ☐ For hierarchical and complex designs, identification of the appropriate level for tests and full reporting of outcomes
- ☒ ☐ Estimates of effect sizes (e.g. Cohen's d , Pearson's r), indicating how they were calculated

Our web collection on [statistics for biologists](#) contains articles on many of the points above.

Software and code

Policy information about [availability of computer code](#)

Data collection

Data presented were either taken in a typical imaging facility on a Leica STED SP8 microscope (BIOP, EPFL), acquired on a custom-built standard microscope using Micromanager 1.4 or kindly provided by Prof. T. Huser (Bielefeld)-SIM figure 3, Prof. M. Sauer (Wurzburg) SIM figure 3, Dr. H. Deschout (EPFL Lausanne) SOFI figure 4 and Dr. J. Schmied and Prof. P. Tinnefeld (GATTAquant and LMU) for DNA-Origami nanoruler data..

Data analysis

The algorithm is implemented in MATLAB R2017b (Mathworks) and ImageJ 1.52. All the codes are made available on Github.

For manuscripts utilizing custom algorithms or software that are central to the research but not yet described in published literature, software must be made available to editors/reviewers. We strongly encourage code deposition in a community repository (e.g. GitHub). See the Nature Research [guidelines for submitting code & software](#) for further information.

Data

Policy information about [availability of data](#)

All manuscripts must include a [data availability statement](#). This statement should provide the following information, where applicable:

- Accession codes, unique identifiers, or web links for publicly available datasets
- A list of figures that have associated raw data
- A description of any restrictions on data availability

All data needed to evaluate the conclusions in the paper are present in the paper and/or the Supplementary Materials. Additional data related to this paper may be requested from the authors

Field-specific reporting

Please select the one below that is the best fit for your research. If you are not sure, read the appropriate sections before making your selection.

☒ Life sciences ☐ Behavioural & social sciences ☐ Ecological, evolutionary & environmental sciences

For a reference copy of the document with all sections, see [nature.com/documents/nr-reporting-summary-flat.pdf](https://www.nature.com/documents/nr-reporting-summary-flat.pdf)

Life sciences study design

All studies must disclose on these points even when the disclosure is negative.

| | |
|-----------------|--|
| Sample size | we were not performing a biological study, so sample sizes were chosen to estimate the precision by calculating the standard deviation based on the number of images that we could acquire in reasonable experimental time |
| Data exclusions | no data was excluded unless it contained clear sample preparation artifacts in the case of STED microscopy (air bubble) |
| Replication | all attempts at replication were successful |
| Randomization | data was not split into different groups, we always used all images of a set of experiments |
| Blinding | data was not split into different groups |

Reporting for specific materials, systems and methods

We require information from authors about some types of materials, experimental systems and methods used in many studies. Here, indicate whether each material, system or method listed is relevant to your study. If you are not sure if a list item applies to your research, read the appropriate section before selecting a response.

Materials & experimental systems

| n/a | Involved in the study |
|-------------------------------------|---|
| <input type="checkbox"/> | <input checked="" type="checkbox"/> Antibodies |
| <input type="checkbox"/> | <input checked="" type="checkbox"/> Eukaryotic cell lines |
| <input checked="" type="checkbox"/> | <input type="checkbox"/> Palaeontology |
| <input checked="" type="checkbox"/> | <input type="checkbox"/> Animals and other organisms |
| <input checked="" type="checkbox"/> | <input type="checkbox"/> Human research participants |
| <input checked="" type="checkbox"/> | <input type="checkbox"/> Clinical data |

Methods

| n/a | Involved in the study |
|-------------------------------------|---|
| <input checked="" type="checkbox"/> | <input type="checkbox"/> ChIP-seq |
| <input checked="" type="checkbox"/> | <input type="checkbox"/> Flow cytometry |
| <input checked="" type="checkbox"/> | <input type="checkbox"/> MRI-based neuroimaging |

Antibodies

| | |
|-----------------|---|
| Antibodies used | anti alpha-tubulin antibody (dilution 1:150, clone [DM1a] mouse monoclonal, ab7291, Lot GR310199-6, Abcam); anti alpha-tubulin antibody (dilution 1:100-1:200, clone B-5-1-2 mouse monoclonal ascites fluid, T5168, Lot 047M4760V, Sigma-Aldrich); donkey anti-Mouse IgG (H+L) Highly Cross-Adsorbed Secondary Antibody, Alexa Fluor 647 (0.005 mg ml ⁻¹ , provided by histology core facility (EPFL), A-31571, Invitrogen); donkey anti-Mouse IgG (H+L) Highly Cross-Adsorbed Secondary Antibody, Alexa Fluor 594 (0.005 mg ml ⁻¹ , A-21203, Lot 1820027, Invitrogen); donkey anti-Mouse IgG (H+L) Highly Cross-Adsorbed Secondary Antibody (dilution 1:100, labeled with Abberior Flip 565 and purified as described in Materials and Methods, A16019, Lot 28-167-092613, Invitrogen), goat anti-mouse IgG Abberior Star 635P (0.005-0.01 mg ml ⁻¹ , 2-0002-007-5, Lot 11042018Hp, Abberior), Anti-mouse IgG-Atto594 antibody produced in goat (0.01 mg ml ⁻¹ , 76085, LotBCBW2434, SigmaAldrich), Atto490LS streptavidin (0.01 mg ml ⁻¹ , AD 490LS-61, Lot SA02S25, Atto-tec), Biotin-SP (long spacer) AffiniPure Donkey Anti-Mouse IgG (H+L) (dilution 1:200, provided by histology core facility (EPFL), 715-065-150, Jackson ImmunoResearch) |
| Validation | anti alpha-tubulin antibody (clone [DM1a] mouse monoclonal, ab7291, Abcam) used in HeLa cells, reactive for Homo sapiens (Human) according to manufacturer; anti alpha-tubulin antibody (clone B-5-1-2 mouse monoclonal ascites fluid, T5168, Sigma-Aldrich) used in COS-7 cells, reactive for African green monkey according to manufacturer |

Eukaryotic cell lines

Policy information about [cell lines](#)

| | |
|---------------------|---|
| Cell line source(s) | HeLa cells are from ATCC, COS-7 cells were a kind gift of the Manley lab (EPFL), MEF cells used in ref 29 were provided by Dr Luca Scorrano and U2OS cells used in ref 26 were cell line ACC785 from DSMZ |
| Authentication | none of the cell lines used were authenticated |

Mycoplasma contamination

cell lines were not tested for Mycoplasma contamination

Commonly misidentified lines
(See [ICLAC](#) register)

no commonly misidentified cell lines were used